Neuron

Article

Differential behavioral engagement of inhibitory interneuron subtypes in the zebra finch brain

Highlights

- Heterogeneous roles exist for GABAergic neurons in the songbird premotor circuit HVC
- HVC interneurons form subgroups defined by differential recruitment across behaviors
- Genetically defined interneurons can be distinguished through molecular markers
- Molecular designations can be mapped onto functional subgroups of HVC interneurons

Authors

Ellie Hozhabri, Ariadna Corredera Asensio, Margot Elmaleh, ..., Jordane Dimidschstein, Gord Fishell, Michael A. Long

Correspondence

mlong@med.nyu.edu

In brief

Hozhabri et al. characterize GABAergic interneuron diversity in a zebra finch circuit critical for courtship song production, using population recordings during behavior and single-cell transcriptomics. They begin to assign distinct network functions to molecularly identified cell types, revealing that parvalbumin and somatostatin interneurons are differentially recruited for separate network roles.

Hozhabri et al., 2025, Neuron *113*, 460–470
February 5, 2025
https://doi.org/10.1016/j.neuron.2024.11.003

CellPress

CellPress

Neuron

Article

Differential behavioral engagement of inhibitory interneuron subtypes in the zebra finch brain

Ellie Hozhabri,[1,2] Ariadna Corredera Asensio,[1,2] Margot Elmaleh,[1,2] Jeong Woo Kim,[1,2] Matthew B. Phillips,[1,2] Paul W. Frazel,[1,2] Jordane Dimidschstein,[3] Gord Fishell,[3,4] and Michael A. Long[1,2,5,*]

[1]NYU Neuroscience Institute and Department of Otolaryngology, New York University Langone Medical Center, New York, NY, USA
[2]Center for Neural Science, New York University, New York, NY, USA
[3]Stanley Center for Psychiatric Research, Broad Institute of Harvard and MIT, Cambridge, MA, USA
[4]Department of Neurobiology, Harvard Medical School, Boston, MA, USA
[5]Lead contact
*Correspondence: mlong@med.nyu.edu
https://doi.org/10.1016/j.neuron.2024.11.003

SUMMARY

Inhibitory interneurons are highly heterogeneous circuit elements often characterized by cell biological properties, but how these factors relate to specific roles underlying complex behavior remains poorly understood. Using chronic silicon probe recordings, we demonstrate that distinct interneuron groups perform different inhibitory roles within HVC, a song production circuit in the zebra finch forebrain. To link these functional subtypes to molecular identity, we performed two-photon targeted electrophysiological recordings of HVC interneurons followed by post hoc immunohistochemistry of subtype-specific markers. We find that parvalbumin-expressing interneurons are highly modulated by sensory input and likely mediate auditory gating, whereas a more heterogeneous set of somatostatin-expressing interneurons can strongly regulate activity based on arousal. Using this strategy, we uncover important cell-type-specific network functions in the context of an ethologically relevant motor skill.

INTRODUCTION

Inhibitory interneuron diversity has been proposed to enhance the computational power of neural circuits,[1–4] with different inhibitory motifs thought to mediate distinct network roles.[5–14] Interneuron cell types have been typically investigated using a "bottom-up" approach (from genes to behavior). For example, mammalian neocortical circuit function studies often rely on transgenic methods to separate classes of GABAergic interneurons that differ across developmental programs and gene expression patterns.[15–20] Despite these efforts, our understanding of how inhibitory interneuron classes differentially contribute to behavior and the extent to which their circuit roles can be generalized across networks and species is incomplete. We therefore used a multidisciplinary strategy to perform a "top-down" (from behavior to genes) analysis of inhibitory interneuron function during an ethologically relevant complex behavior: the courtship song of the zebra finch.

Birdsong is mediated by a set of well-characterized brain regions that form the vocal production pathway, including the key forebrain nucleus HVC (proper name).[21,22] HVC acts as a crucial sensorimotor hub, integrating motor thalamic,[23–25] auditory,[26–28] and neuromodulatory[29,30] inputs. Several lines of evidence have highlighted the central importance of HVC for generating premotor signals that directly control the pacing of song.[22,31,32] Because of the clear relationship between circuit activity and behavioral performance, HVC therefore offers the opportunity to determine precise sensorimotor roles for different circuit elements. Of interest to this study are local GABAergic interneurons, which account for ~15% of the HVC circuit,[33,34] forming dense, reciprocal connections with excitatory projection cells.[35–37] Although HVC interneurons have been historically considered a single, monolithic cell class in models of network function,[37–41] a close inspection of previous literature reveals hints of diversity across HVC GABAergic neurons,[34,42–45] including a recent report in which a variety of transcriptomically defined classes of HVC interneurons was described.[34] How specific circuit functions correspond to these molecular determinants remains unknown.

RESULTS

Multiple roles for HVC inhibition

Within HVC (Figure 1A), several roles for inhibition have been proposed, including contributing to[36,40]—or even directly establishing[46]—motor-related sequences, regulating sensory input,[47,48] and modulating population activity across arousal states.[44,45] These findings have largely been inferred from indirect observations, such as responses to pharmacological interventions[36] or electrophysiological methods that are unable to measure inhibitory currents.[32,42] We therefore performed *in vivo* whole-cell voltage-clamp recordings in HVC excitatory projection neurons

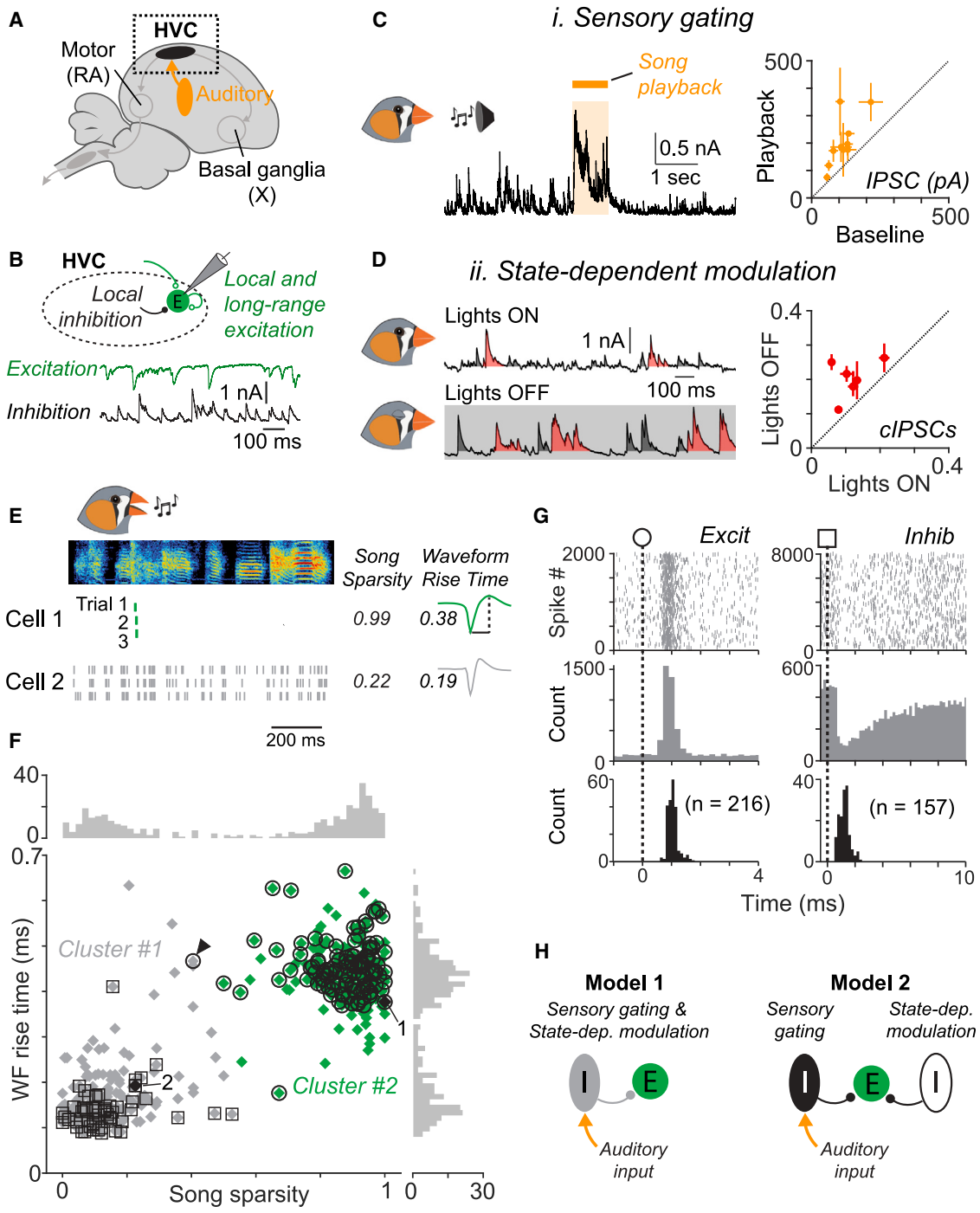

Figure 1. Diverse roles for inhibition in zebra finch HVC

(A) Schematic of zebra finch brain highlighting the premotor nucleus HVC and associated output nuclei and auditory afferents.

(B) *In vivo* whole-cell recording of HVC projection neurons can reveal excitatory and inhibitory synaptic currents.

(C) Sensory gating: inhibitory currents are driven by song playback for an individual neuron (left) and across the population (right, $n = 10$ cells).

(D) State-dependent modulation: spontaneous inhibitory postsynaptic currents recorded across different lighting conditions for a single neuron (left). The proportion of compound inhibitory postsynaptic currents (cIPSCs, see STAR Methods) increased in the lights OFF condition ($n = 6$ cells) (right). Error bars in (C) and (D) represented as standard deviation.

(E) Activity of two example neurons simultaneously recorded from bird C22 during three song trials. Spike waveforms at right (rise time indicated in ms).

(F) Scatterplot showing spike shape and song sparsity (see STAR Methods) for 368 neurons from five birds. Population divided into two groups (indicated by gray and green) using k-means clustering (k = 2). Histogram axes are displayed as counts.

(legend continued on next page)

(n = 12 neurons in 5 birds) to understand the postsynaptic consequences of the HVC inhibitory network. By holding the membrane potential near the reversal values for excitation (1.4 ± 3.5 mV) or inhibition (−67.8 ± 4.9 mV), we isolated inhibitory and excitatory currents, respectively (Figure 1B; see STAR Methods).

Given the technical limitations of assessing singing activity under head-fixed, microscopy-guided intracellular recording conditions, we narrowed our focus to two other primary roles for synaptic inhibition within the HVC circuit: "sensory gating" and "state-dependent modulation" of network function. For sensory gating, specifically related to auditory inputs, we examined changes in inhibitory currents resulting from exposure to the bird's own song.[49] Song playback led to increased inhibitory current (mean change: 83% ± 61%) compared with baseline values (Figure 1C, p = 0.002, Wilcoxon signed-rank test, n = 10 neurons), consistent with previous work demonstrating that HVC interneurons receive auditory afferents.[24,26–28] State-dependent modulation has been well documented in the zebra finch, with profoundly different activity occurring during wake and sleep (e.g., Figures S4E and S4F).[50,51] We examined the profile of inhibitory events after turning off the light in the recording arena, a manipulation that reliably evokes sleep in zebra finches.[52] In the Lights OFF condition, inhibitory currents often formed long-lasting complex events (Figure 1D; see STAR Methods), whose incidence increased by 99.7% ± 14.3% compared with the Lights ON condition (Figure 1D, p = 0.031, Wilcoxon signed-rank test, n = 6 neurons). Such modulation did not happen immediately, and when lights were turned on and off with a faster (~30-s) duty cycle, compound inhibitory events did not significantly change (−18.9% ± 31% OFF relative to ON, p = 0.375, Wilcoxon signed-rank test, n = 4 neurons), supporting the notion that these events were due not simply to changes in visual stimulation but to a longer timescale physiological response, such as arousal.[45,51] Taken together, these inhibitory current measurements demonstrate that sensory-driven playback responses and arousal-related (i.e., lights ON/OFF) changes in inhibitory currents can be observed in HVC excitatory neurons and suggest that such changes in inhibitory tone may regulate neuronal output across behavioral states.

To further characterize the source of inhibition within HVC, we analyzed individual activity profiles of local HVC inhibitory neurons during behavior. Using chronic silicon probe recordings,[39,53] we first differentiated inhibitory interneurons from excitatory cells based on narrow spike waveforms and song sparsity (Figures 1E and 1F; see STAR Methods).[36,37,54] We then performed k-means clustering to group neurons into two populations whose profiles matched inhibitory (n = 155, Figure 1F, gray) and excitatory (n = 213, Figure 1F, green) neurons. We additionally assessed whether potential inhibitory/excitatory connections between simultaneously recorded neurons could further confirm their identity. To accomplish this, we carried out a spike cross-correlation analysis that uncovered potential excitatory (n = 216 pairs involving 117 putative presynaptic neurons) and inhibitory (n = 157 pairs involving 59 putative presynaptic neurons) connections (Figures 1G and S1). These connectivity-based designations confirmed our original cell-type classifications in 175 out of 176 cases (99.4%), thus validating our strategy for identifying HVC inhibitory interneurons.

We tested two models regarding the circuit roles of HVC interneurons. First, the possibility exists that diverse network functions, such as sensory gating and state-dependent modulation, may be the product of a single cell class broadly involved in all inhibitory roles within that circuit (model 1; Figure 1H). Alternately, each interneuron circuit role may be mediated by dedicated inhibitory cell classes that are selectively responsible for different network functions (model 2; Figure 1H). To address these models, we analyzed individual activity profiles of identified HVC inhibitory neurons in the behaving zebra finch.

Functional properties of HVC inhibitory interneurons

Our models (Figure 1H) provide specific predictions (Figure 2A) concerning the recruitment of HVC interneurons. Model 1 suggests that all interneurons should be consistently recruited across behaviors (prediction #1). Alternatively, model 2 posits a more heterogeneous function within the collective HVC interneuron pool, and different interneurons should exhibit different roles within the network. This division of labor need not be categorical, and different neurons may be variably recruited by different behaviors, distributing the responsibility for each computation broadly across the population (prediction #2). A third possibility is that interneurons are clustered into more than one functional class, with each subpopulation exhibiting its own distinct behavioral profile (prediction #3). By characterizing how inhibitory interneurons contribute to an identified circuit responsible for generating a complex behavior, we will test these possibilities.

We assessed network-related activity profiles of interneurons by recording their auditory-evoked responses during song playback (Figures 2B and S2A), spontaneous spiking activity across different levels of arousal (Figures 2C and S2B), and changes in spiking rate during singing (Figures 2D and S2C). We aligned the activity of individual neurons across trials, which revealed highly heterogeneous responses, inconsistent with a model in which all inhibitory interneurons are uniformly recruited across behavioral conditions (Figure 2A, prediction #1). We therefore tested the alternate hypotheses in which HVC interneurons are differentially responsive across behaviors (Figure 2A, prediction #2 or #3). We measured responses to playback, song production, and arousal changes (Figure 2E; see STAR Methods) and performed a k-means clustering analysis using these parameters. We found five clusters of interneurons using two different cluster optimization methods (Figures 2F and 2G; Calinski-Harabasz score: 93.9; silhouette score: 56.0), inconsistent with a broad and distributed

Circles and squares in (F) represent putative presynaptic excitatory and inhibitory neurons, respectively, based on analysis in (G), and black arrow represents a single case in which the two cell identification methods were not in agreement.

(G) Two examples of spiking cross-correlations showing putative excitatory (left) and inhibitory (right) synaptic interactions along with the timing of maxima (excitatory, 1.05 ± 0.18 ms) and minima (inhibitory, 1.22 ± 0.36 ms) values across all putative connections.

(H) Inhibition may arise either from a monolithic inhibitory cell class (model 1) or from unique functional groups of inhibitory cells (model 2).

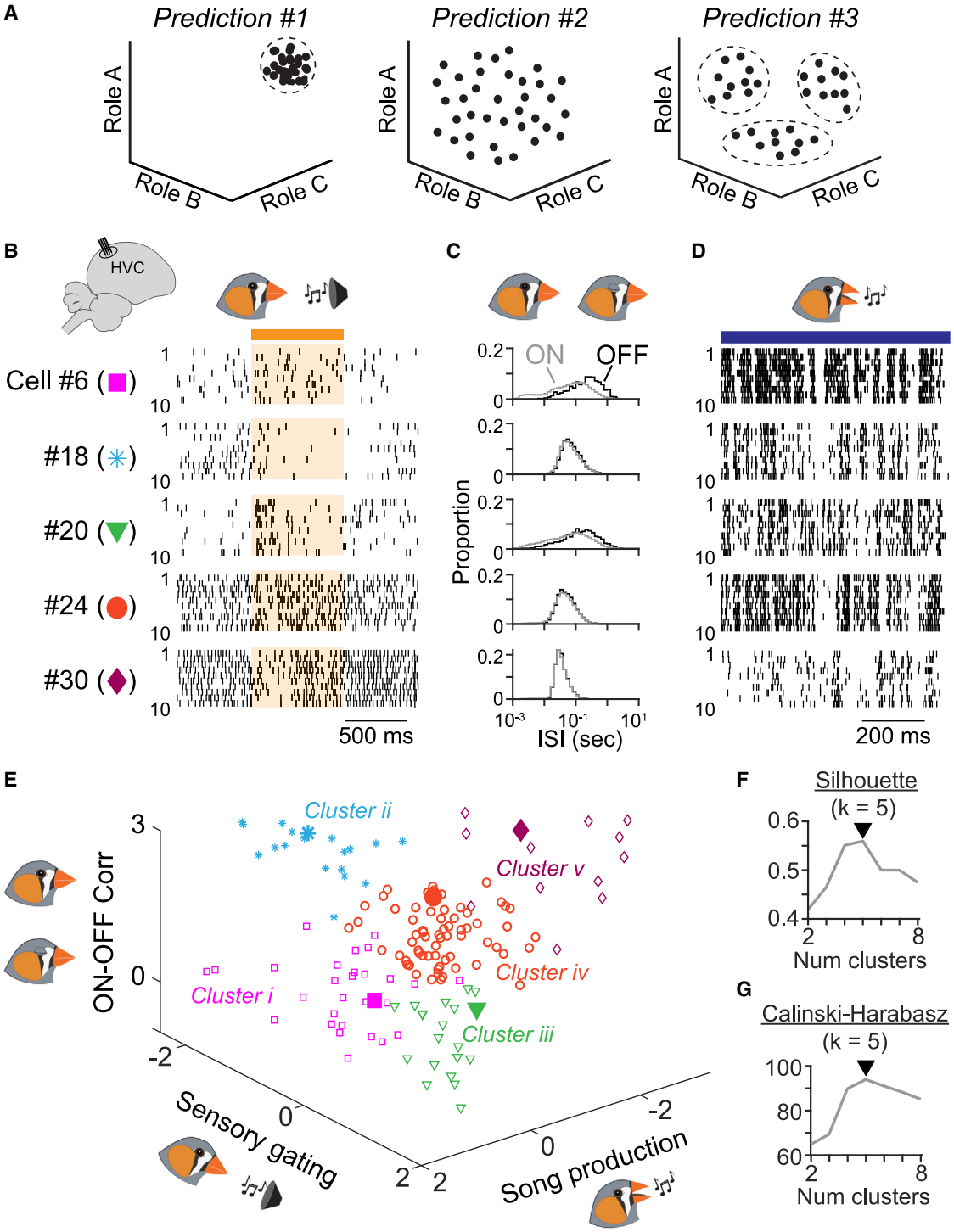

Figure 2. Population dynamics of HVC interneurons

(A) Three possible outcomes for the distribution of network responses of HVC interneurons.

(B–D) Spiking activity aligned to playback (B), histograms of interspike intervals in Lights ON (gray) and Lights OFF (black) conditions (C), and spiking activity during singing (D) for 5 example HVC interneurons recorded with silicon probe arrays (see schematic, left). Rows of spiking activity in (B) and (D) correspond to single trials.

(legend continued on next page)

functional representation of inhibitory interneurons (Figure 2A, prediction #2). Among these five clusters, we noted heterogeneity in recruitment for different network functions. For instance, cluster ii interneurons display strong playback-evoked responses but do not modulate their firing rates across lighting conditions (e.g., cluster i) or during singing (e.g., cluster v) (Figure 2E). We also observed five clusters when the same analysis was performed with three alternative measurements of song-related activity (Figure S2D). In summary, our chronic silicon probe recordings in freely behaving birds reveal that HVC interneurons represent a highly heterogeneous population and that functional subgroups of interneurons can preferentially participate in distinct network roles (Figure 2A, prediction #3).

Molecular diversity of HVC interneurons

We next aimed to establish whether functionally defined groups of interneurons correspond to different molecular classes.[34] To characterize the molecular profile of HVC interneurons, we performed single-nucleus mRNA sequencing in the zebra finch (Figure 3), yielding 11,637 distinct transcriptomes (n = 3 birds, Figures S3A–S3E; see STAR Methods). We focused our attention on GABAergic clusters (1,764 cells), which were distinguished by significant expression of GAD1 (Figure 3A) as well as GAD2 and VGAT (Figure S3F). Previous work, including in the finch,[34] that inhibitory interneurons can be subdivided into canonical classes based on developmental origins across amniotes, such as the medial ganglionic eminence (MGE), the caudal ganglionic eminence (CGE), and the lateral ganglionic eminence (LGE),[16,18,34] and this study confirms this organizing principle (Figures 3B–3D).

We focused on three transcriptomic clusters (clusters 1, 2, and 5) that expressed canonical markers of MGE-derived cells (Figures 3B–3E) because they represent the largest developmental group present in our dataset (44% of GAD1+ cells; n = 784 neurons) and because of their evolutionary correspondence to major cardinal classes found in the mammalian neocortex (i.e., MGE-derived parvalbumin [PV] and somatostatin [SST] classes) (Figure 3E).[16,17,34] Consistent with previous work from another group,[34] our top differentiating gene of cluster 5 was *PVALB* (corresponding to PV), whereas *SST* was strongly expressed in clusters 1 and 2 and was a top differentiating gene in cluster 1 (Figures 3C and 3D). Using antibody labeling, we confirmed that HVC neurons often expressed PV, SST, and sometimes both markers simultaneously (Figures 3F and 3G). We can therefore use immunohistochemistry to broadly distinguish MGE-derived interneurons as well as specific subgroups within this overarching classification.

Molecular signatures of functionally distinct interneuron subtypes

We next aimed to understand whether the functional diversity of HVC interneurons uncovered in this study (Figure 2) relates to the molecular classifications from our transcriptomic analysis (Figure 3). Guided by a related approach[55] in the mammalian brain, we attempted to achieve this critical linkage of molecular and functional diversity by coupling two-photon guided juxtacellular recordings with retrospective histological profiling of recorded interneurons in the songbird. We first labeled HVC interneurons (Figure 4A) using a virus (AAV-Dlx-GFP) capable of selectively targeting GABAergic neurons, including those derived from MGE,[56] but excluding specific classes such as the LGE-derived population (i.e., Figures 3C and 3D, cluster 0). We then used a complementary post hoc method to assay subtype-specific molecular markers for recorded cells (Figures 4B–4D and S4A–S4F), following previous studies[57–61] that used image registration to locate the same neurons recorded *in vivo* and in histological slices, so that immunostaining or other assays could be performed. We followed a similar two-step protocol that allowed us to connect functional and molecular designations within a single neuron (e.g., Figures 4C and 4D). To optimize the registration of *in vivo* and histological image stacks, we sliced whole brains tangentially (i.e., parallel to the imaging plane) and relied on common landmarks visible in both contexts, including blood vessels and constellations of sparsely labeled neurons (e.g., Figure 4B). In total, we performed *in vivo* juxtacellular recordings from 59 GFP+ neurons from 30 birds, and we recovered 20 of these neurons after immunostaining for PV and SST (Figure 4D), a strategy that should label a subset of the 8 molecularly defined interneuron subclasses[34] in HVC (Figure 3). With this combined approach, we were able to access both the network-level electrophysiological properties of distinct GABAergic interneurons as well as their corresponding molecular identities.

To describe the functional properties of juxtacellularly recorded interneurons, we quantified the trough-to-peak rise time of the average spike waveform (Figure 4E), auditory-evoked responses to song playback (Figure 4F), and correspondence of spontaneous firing patterns across lighting conditions (Figure 4G) (see STAR Methods), akin to the quantifications made with the silicon probe dataset (Figure 2). We found similar cell responses across these recording modalities (Figures S4G and S4H), including a large degree of physiological heterogeneity (Figures 2H and 4I). SST+ neurons were consistent across all three parameters, regardless of whether PV was co-expressed (Figure S4I, $p > 0.15$, Wilcoxon rank-sum test). We therefore combined SST+/PV− with SST+/PV+ as a single class, referred to for the remainder of this study as simply "SST." Compared with SST neurons, PV neurons exhibited narrower spike waveforms (PV: 0.22 ± 0.03 ms, SST: 0.31 ± 0.07 ms, p = 0.019, Wilcoxon rank-sum test) and showed large spike-rate changes in response to playback (PV: 0.59 ± 0.09, SST: 0.29 ± 0.09, p = 0.00032, Wilcoxon rank-sum test) compared with SST neurons. Accordingly, every PV cell was significantly modulated by song playback (p = 0.0011, Wilcoxon signed-rank test). SST neurons showed heterogeneous state-dependent modulation, with some of these neurons strongly changing their firing with arousal,

(E) HVC interneurons (n = 155 from 5 birds) were clustered based on network properties using k-means clustering. "ON-OFF correlation" is the correlation between ISI histograms in light and dark conditions (measure of state-dependent modulation), and "sensory gating" and "song production" refer to the change in spike rate resulting from song playback and singing, respectively (see STAR Methods). Axes are normalized (see STAR Methods). Example neurons from (B)–(D) indicated with larger filled icons.
(F and G) Silhouette (F) and Calinski-Harabasz (G) analyses were used to determine the optimal number of clusters (k = 5).

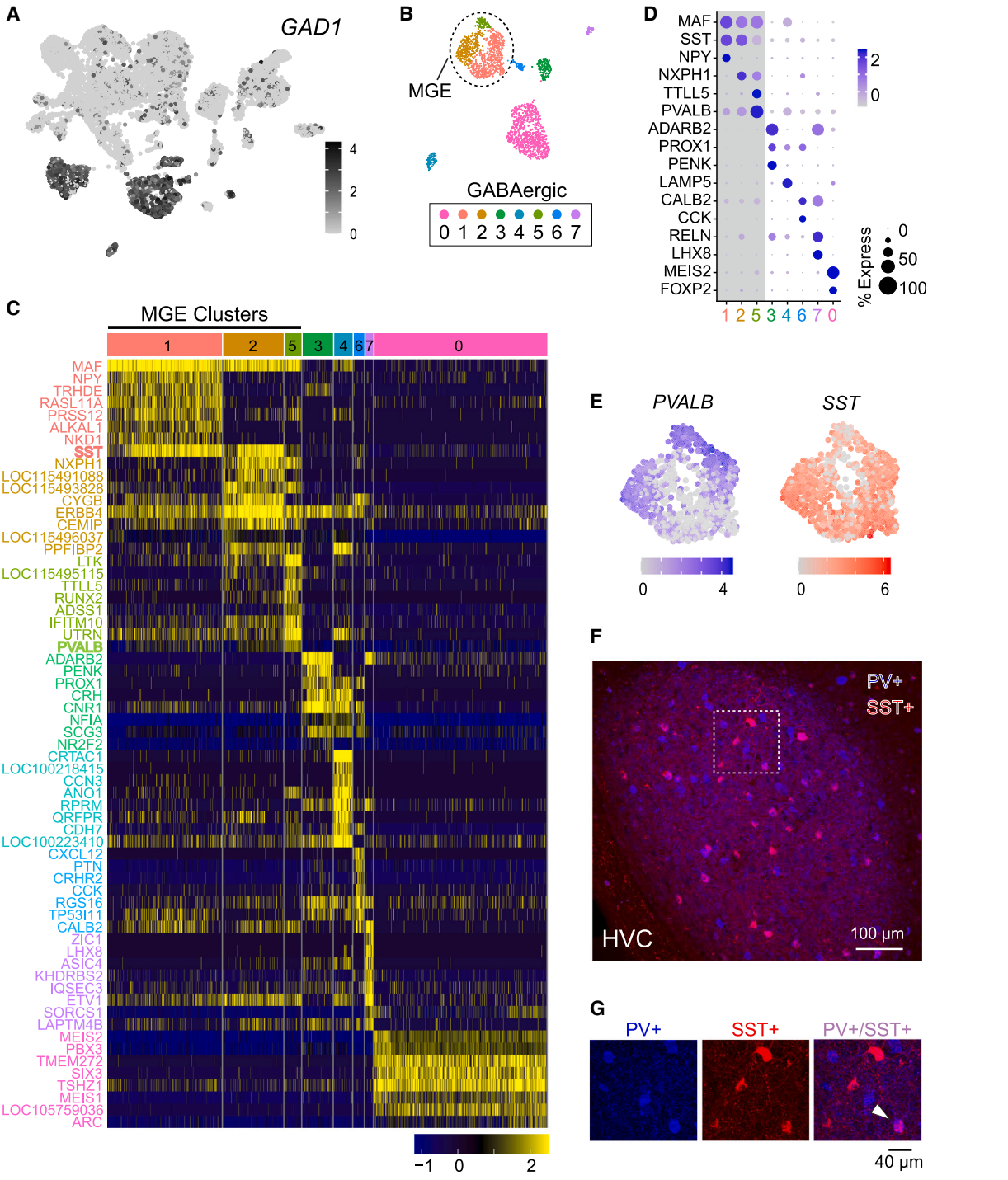

Figure 3. Defining HVC inhibitory interneurons

(A) Uniform manifold approximation and projection (UMAP) representation of clusters from 11,637 single-nucleus transcriptomes indicating expression level of GABAergic marker *GAD1*. Scale bar indicates expression levels scaled to the maximum expression value of the *GAD1* gene.

(B) UMAP representation of GABAergic clusters, with a subpopulation expressing genes consistent with MGE origin (circled).

(C) Heatmap illustrating normalized expression levels of the top eight most differentiating features for all eight GABAergic clusters. Gene expression patterns suggest varying developmental origins among clusters, such as MGE (clusters 1, 2, and 5)-, CGE (clusters 3, 4, and 6)-, and LGE (cluster 0)-derived neurons. In bold, PVALB (i.e., PV) and SST genes were found among top markers for two unique MGE clusters.

(legend continued on next page)

leading to lower correlation values of ISI distributions (see STAR Methods) across lighting conditions (SST: 0.70 ± 0.31, PV: 0.94 ± 0.07).

When all three parameters were plotted for histologically recovered cells, we observed that PV and SST neurons occupied nonoverlapping areas within this functional space (Figure 4I), and clustering was also observed when plotting pairs of each of these parameters in two dimensions (Figure S4I). The distance between neurons within the same category (i.e., PV↔PV) was significantly smaller than across categories or between randomly selected pairs regardless of label (Figure 4J), indicating separable functional roles for these genetic cell classes. Additionally, we recovered neurons that did not exhibit any labeling (i.e., PV−/SST− cells), which were found to be neither playback responsive nor state modulated and thus also closely spaced functionally (Figure 4I), and likely represent other transcriptomic clusters (e.g., CGE-derived classes, Figures 3C and 3D) that we did not assay in this experiment. In conclusion, we find that cells that share similar behaviorally relevant functional responses can also share a common molecular profile and that these functions can be defined using behavioral (i.e., top-down) rather than cell-autonomous (i.e., bottom-up) features.

DISCUSSION

Our work parallels recent experiments in mouse aimed at linking *in vivo* activity onto molecularly defined subtypes in the retina,[62] hippocampus,[63] visual cortex,[64] and somatosensory cortex.[65] Unlike the mouse, the songbird enables us to clearly categorize the roles of different interneuron types during the performance of a rich, circuit-driven natural behavior. These results challenge existing models of HVC network function that presently rely on a single interneuron type within that structure.[37–41] Instead, we find five functionally distinct clusters by examining responses to song, sensory gating, and sleep-wake state modulation. Future work will determine whether further functional clusters can be identified when expanding our view to consider additional behavioral conditions (e.g., sleep replay[50,53]) or different developmental stages (e.g., song learning[48]).

Here, we take the first step toward testing whether conserved populations of interneurons across distantly related species may mediate similar functions. We find that the activity of PV neurons in the zebra finch brain was strongly modulated during song playback (Figure 4F, 4H, and 4K), consistent with a sensory gating role for this population in the HVC network,[44,45,47,48] perhaps regulating instructive inputs during song learning.[48] Other studies carried out in the mammalian forebrain have supported this notion by indicating that PV cells often mediate feed-forward inhibition[3,66,67] that gates the impact of sensory inputs to a circuit. Additionally, we find that SST interneurons are more functionally heterogeneous than PV interneurons, which may be related to the finding that SST neurons in other systems are highly diverse.[68–71] Also, SST neurons in the rodent brain are often sensitive to neuromodulators,[72,73] potentially mediating the arousal changes we observe in our dataset (Figures 4G, 4H, and 4K). The similarities between avian and mammalian interneuron functions are surprising, given the evolutionary distance of ~320 million years and the lack of a laminar architecture (i.e., neocortical layers), which often correspond strongly to interneuron network roles in the mammalian brain.[71]

Our top-down strategy of establishing behavioral clusters and then identifying the molecules associated with these functional groups has many advantages. Because bottom-up approaches can lead to seemingly irreconcilable differences in interpretation (e.g., lumping vs. splitting of cell-type designations), behavioral analyses such as those introduced here can provide much-needed clarification.[1,74] Nevertheless, a more complete bottom-up analysis[20,75] could also provide complementary information that can help to bridge the gap between the avian brain and established mammalian datasets. Additionally, new reagents designed to label inhibitory subpopulations across species[76] as well as emerging multi-omics approaches[77] may help to functionally characterize other inhibitory subtypes recently found to exist in the zebra finch song production pathway,[34] including those neurons derived from the LGE (i.e., cluster 0, FOXP2+ interneurons). Taken together, our top-down approach revealed that functional subgroups of HVC interneurons could successfully map onto molecular classes (Figure 3). Although others have used this behavior-first approach to investigate well-defined laboratory tasks in genetically tractable model systems,[78] broadening these efforts could further elucidate how individual circuit elements are engaged across a range of ethologically relevant brain processes.

RESOURCE AVAILABILITY

Lead contact

Further information and requests for resources and reagents should be directed to and will be fulfilled by the lead contact, Michael Long (mlong@med.nyu.edu).

Materials availability

This study did not generate new, unique reagents.

Data and code availability

Key analysis code is available at https://github.com/hozhabrie/HVC_Interneuron_Analysis. The datasets generated during this study and any additional information required to reanalyze the data reported in this paper are available upon request from the lead contact.

ACKNOWLEDGMENTS

We thank Dmitiry Aronov, Arkarup Banerjee, Robert Machold, Felix Moll, Robin Tremblay, Nicolas Tritsch, and members of the Long laboratory for comments on earlier versions of this manuscript. Abby Paulson provided technical

(D) Representative genes of 8 clusters shown in (B).
(E) UMAP plot of MGE-derived interneurons that differentially express *PVALB* (left) and *SST* (right). Scale bars indicate expression levels scaled to the maximum expression value of each gene.
(F) Immunostaining showing PV and SST expression in HVC.
(G) A magnified view of a portion of HVC showing neurons singly labeled with PV and SST and cells co-labeled by both markers (bottom). White arrow indicates example of co-labeled cell.

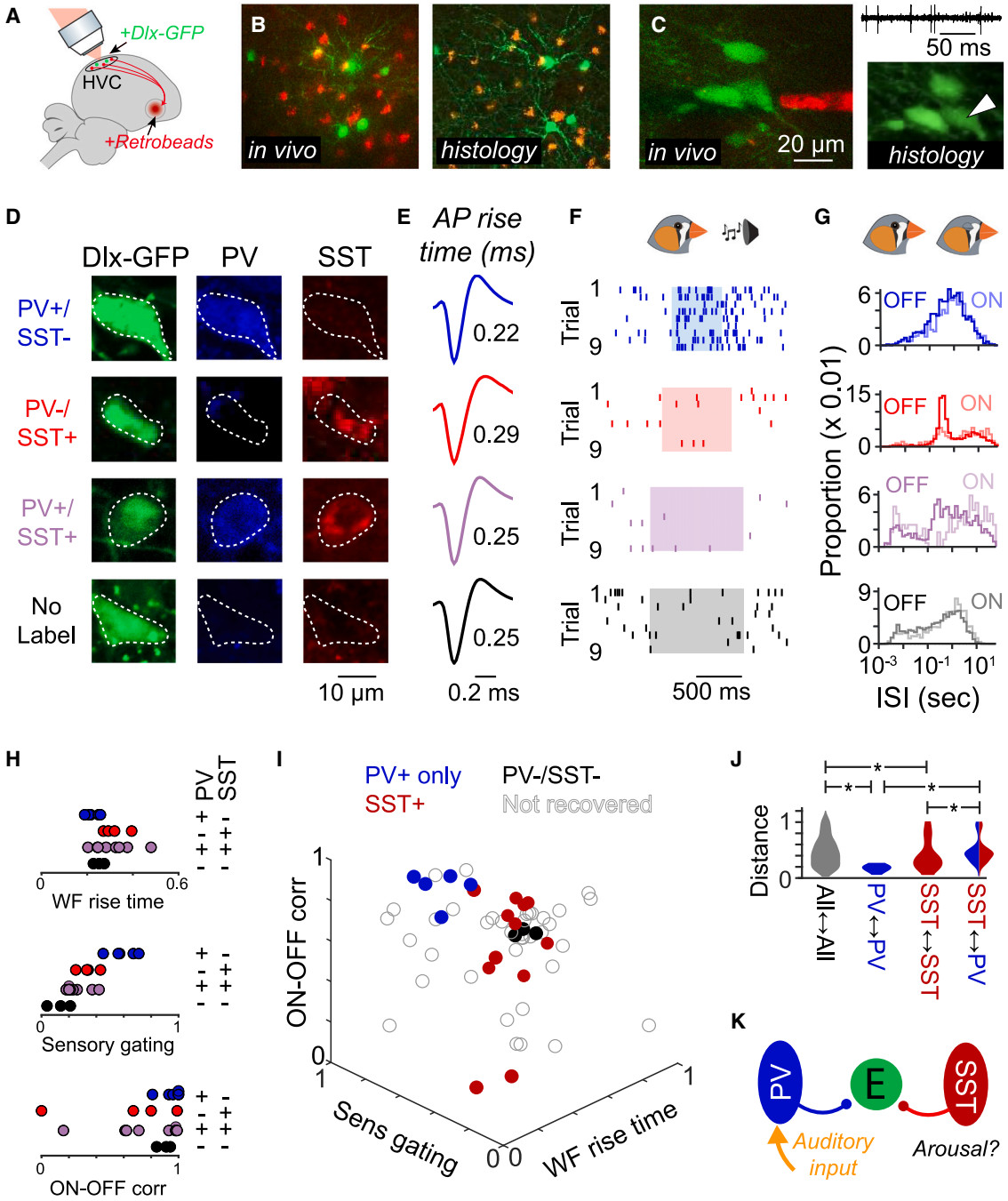

Figure 4. Functionally distinct inhibitory cell types express different molecular markers

(A) Schematic of the *in vivo* recording configuration. Dlx-GFP and red Retrobeads were injected into HVC and area X, respectively.

(B) A view of the same HVC neurons imaged both *in vivo* and in a histological slice (see STAR Methods).

(C) A GFP-expressing neuron recorded *in vivo* under two-photon guidance (pipette in red). Representative spiking at upper right (amplitude: 0.6 mV). At lower right, an image of visually targeted neurons recovered histologically.

(D) Examples of histologically recovered neurons labeled differentially with PV and SST. PV example indicated with white arrow in (C).

(E–G) Waveform (WF) rise times (E), song playback responses (F), and histograms of interspike intervals (G) for the neurons shown in (D).

(H) Values for sensory gating, WF rise time, and ON-OFF correlation for PV+/SST−, PV−/SST+, PV+/SST+ neurons. "ON-OFF correlation" is the correspondence of ISI in light and dark conditions, and "sensory gating" refers to the absolute change in spike rate resulting from song playback (see STAR Methods).

(legend continued on next page)

assistance, and the NYU Genome Technology Center helped with transcriptomics. We acknowledge helpful conversations with Chiung-Yin Chung, Robert Machold, Sean Kelly, and Maria Tosches. Our work was funded by the National Institutes of Health (R01 NS075044, M.A.L.) and the Simons Collaboration on the Global Brain (M.A.L.).

AUTHOR CONTRIBUTIONS

Conceptualization, E.H. and M.A.L.; methodology, E.H., A.C.A., M.E., M.B.P., P.W.F., and M.A.L.; visualization, E.H., A.C.A., J.W.K., M.B.P., P.W.F., and M.A.L.; analysis, E.H., M.E., J.W.K., and M.A.L.; funding acquisition, M.A.L.; project administration, M.A.L.; supervision, M.A.L.; reagents, J.D. and G.F.; writing – original draft, E.H. and M.A.L.; writing – review & editing, E.H., A.C.A., M.E., M.B.P., P.W.F., G.F., and M.A.L.

DECLARATION OF INTERESTS

The authors declare no competing interests.

STAR★METHODS

Detailed methods are provided in the online version of this paper and include the following:

- KEY RESOURCES TABLE
- EXPERIMENTAL MODEL AND STUDY PARTICIPANT DETAILS
- METHOD DETAILS
  - Surgical approaches
  - Experimental approaches
  - Whole-cell analysis
  - Silicon probe analysis
  - Transcriptomics analysis
  - Juxtacellular analysis
- QUANTIFICATION AND STATISTICAL ANALYSIS

SUPPLEMENTAL INFORMATION

Supplemental information can be found online at https://doi.org/10.1016/j.neuron.2024.11.003.

Received: May 18, 2024
Revised: August 30, 2024
Accepted: November 7, 2024
Published: December 6, 2024

REFERENCES

1. Fishell, G., and Kepecs, A. (2020). Interneuron Types as Attractors and Controllers. Annu. Rev. Neurosci. *43*, 1–30. https://doi.org/10.1146/annurev-neuro-070918-050421.
2. Kepecs, A., and Fishell, G. (2014). Interneuron cell types are fit to function. Nature *505*, 318–326. https://doi.org/10.1038/nature12983.
3. Tremblay, R., Lee, S., and Rudy, B. (2016). GABAergic Interneurons in the Neocortex: From Cellular Properties to Circuits. Neuron *91*, 260–292. https://doi.org/10.1016/j.neuron.2016.06.033.
4. Roux, L., and Buzsáki, G. (2015). Tasks for inhibitory interneurons in intact brain circuits. Neuropharmacology *88*, 10–23. https://doi.org/10.1016/j.neuropharm.2014.09.011.
5. Pi, H.J., Hangya, B., Kvitsiani, D., Sanders, J.I., Huang, Z.J., and Kepecs, A. (2013). Cortical interneurons that specialize in disinhibitory control. Nature *503*, 521–524. https://doi.org/10.1038/nature12676.
6. Vu, E.T., and Krasne, F.B. (1992). Evidence for a computational distinction between proximal and distal neuronal inhibition. Science *255*, 1710–1712. https://doi.org/10.1126/science.1553559.
7. Wehr, M., and Zador, A.M. (2003). Balanced inhibition underlies tuning and sharpens spike timing in auditory cortex. Nature *426*, 442–446. https://doi.org/10.1038/nature02116.
8. Hartline, H.K., Wagner, H.G., and Ratliff, F. (1956). Inhibition in the eye of Limulus. J. Gen. Physiol. *39*, 651–673. https://doi.org/10.1085/jgp.39.5.651.
9. Ferrante, M., Migliore, M., and Ascoli, G.A. (2009). Feed-forward inhibition as a buffer of the neuronal input-output relation. Proc. Natl. Acad. Sci. USA *106*, 18004–18009. https://doi.org/10.1073/pnas.0904784106.
10. Basu, J., Zaremba, J.D., Cheung, S.K., Hitti, F.L., Zemelman, B.V., Losonczy, A., and Siegelbaum, S.A. (2016). Gating of hippocampal activity, plasticity, and memory by entorhinal cortex long-range inhibition. Science *351*, aaa5694. https://doi.org/10.1126/science.aaa5694.
11. Gabernet, L., Jadhav, S.P., Feldman, D.E., Carandini, M., and Scanziani, M. (2005). Somatosensory integration controlled by dynamic thalamocortical feed-forward inhibition. Neuron *48*, 315–327. https://doi.org/10.1016/j.neuron.2005.09.022.
12. Silberberg, G., and Markram, H. (2007). Disynaptic inhibition between neocortical pyramidal cells mediated by Martinotti cells. Neuron *53*, 735–746. https://doi.org/10.1016/j.neuron.2007.02.012.
13. Kapfer, C., Glickfeld, L.L., Atallah, B.V., and Scanziani, M. (2007). Supralinear increase of recurrent inhibition during sparse activity in the somatosensory cortex. Nat. Neurosci. *10*, 743–753. https://doi.org/10.1038/nn1909.
14. Adesnik, H., Bruns, W., Taniguchi, H., Huang, Z.J., and Scanziani, M. (2012). A neural circuit for spatial summation in visual cortex. Nature *490*, 226–231. https://doi.org/10.1038/nature11526.
15. Gouwens, N.W., Sorensen, S.A., Berg, J., Lee, C., Jarsky, T., Ting, J., Sunkin, S.M., Feng, D., Anastassiou, C.A., Barkan, E., et al. (2019). Classification of electrophysiological and morphological neuron types in the mouse visual cortex. Nat. Neurosci. *22*, 1182–1195. https://doi.org/10.1038/s41593-019-0417-0.
16. Tasic, B., Menon, V., Nguyen, T.N., Kim, T.K., Jarsky, T., Yao, Z., Levi, B., Gray, L.T., Sorensen, S.A., Dolbeare, T., et al. (2016). Adult mouse cortical cell taxonomy revealed by single cell transcriptomics. Nat. Neurosci. *19*, 335–346. https://doi.org/10.1038/nn.4216.
17. Tasic, B., Yao, Z., Graybuck, L.T., Smith, K.A., Nguyen, T.N., Bertagnolli, D., Goldy, J., Garren, E., Economo, M.N., Viswanathan, S., et al. (2018). Shared and distinct transcriptomic cell types across neocortical areas. Nature *563*, 72–78. https://doi.org/10.1038/s41586-018-0654-5.
18. Tosches, M.A., Yamawaki, T.M., Naumann, R.K., Jacobi, A.A., Tushev, G., and Laurent, G. (2018). Evolution of pallium, hippocampus, and cortical cell types revealed by single-cell transcriptomics in reptiles. Science *360*, 881–888. https://doi.org/10.1126/science.aar4237.
19. Mayer, C., Hafemeister, C., Bandler, R.C., Machold, R., Batista Brito, R., Jaglin, X., Allaway, K., Butler, A., Fishell, G., and Satija, R. (2018). Developmental diversification of cortical inhibitory interneurons. Nature *555*, 457–462. https://doi.org/10.1038/nature25999.
20. Yao, Z., van Velthoven, C.T.J., Nguyen, T.N., Goldy, J., Sedeno-Cortes, A.E., Baftizadeh, F., Bertagnolli, D., Casper, T., Chiang, M., Crichton, K., et al. (2021). A taxonomy of transcriptomic cell types across the isocortex

(I) Functional properties of all juxtacellularly recorded HVC interneurons (n = 59 from 30 birds). Filled icons (n = 20) represent histologically recovered neurons. Color coded in legend.
(J) Distance between neurons in (I) is greater both across classes (PV-SST) and in randomly assigned pairs compared with within class (e.g., PV-PV) pairs (* $p < 0.05$, Wilcoxon rank-sum test).
(K) PV interneurons preferentially receive auditory input, whereas SST interneurons can exhibit state-dependent changes in their firing properties.

and hippocampal formation. Cell *184*, 3222–3241.e26. https://doi.org/10.1016/j.cell.2021.04.021.

21. Nottebohm, F., Stokes, T.M., and Leonard, C.M. (1976). Central control of song in the canary, Serinus canarius. J. Comp. Neurol. *165*, 457–486. https://doi.org/10.1002/cne.901650405.
22. Hahnloser, R.H.R., Kozhevnikov, A.A., and Fee, M.S. (2002). An ultrasparse code underlies the generation of neural sequences in a songbird. Nature *419*, 65–70. https://doi.org/10.1038/nature00974.
23. Moll, F.W., Kranz, D., Corredera Asensio, A., Elmaleh, M., Ackert-Smith, L.A., and Long, M.A. (2023). Thalamus drives vocal onsets in the zebra finch courtship song. Nature *616*, 132–136. https://doi.org/10.1038/s41586-023-05818-x.
24. Nottebohm, F., Kelley, D.B., and Paton, J.A. (1982). Connections of vocal control nuclei in the canary telencephalon. J. Comp. Neurol. *207*, 344–357. https://doi.org/10.1002/cne.902070406.
25. Coleman, M.J., Roy, A., Wild, J.M., and Mooney, R. (2007). Thalamic gating of auditory responses in telencephalic song control nuclei. J. Neurosci. *27*, 10024–10036. https://doi.org/10.1523/JNEUROSCI.2215-07.2007.
26. Zhao, W., Garcia-Oscos, F., Dinh, D., and Roberts, T.F. (2019). Inception of memories that guide vocal learning in the songbird. Science *366*, 83–89. https://doi.org/10.1126/science.aaw4226.
27. Roberts, T.F., Hisey, E., Tanaka, M., Kearney, M.G., Chattree, G., Yang, C.F., Shah, N.M., and Mooney, R. (2017). Identification of a motor-to-auditory pathway important for vocal learning. Nat. Neurosci. *20*, 978–986. https://doi.org/10.1038/nn.4563.
28. Akutagawa, E., and Konishi, M. (2010). New brain pathways found in the vocal control system of a songbird. J. Comp. Neurol. *518*, 3086–3100. https://doi.org/10.1002/cne.22383.
29. Tanaka, M., Sun, F., Li, Y., and Mooney, R. (2018). A mesocortical dopamine circuit enables the cultural transmission of vocal behaviour. Nature *563*, 117–120. https://doi.org/10.1038/s41586-018-0636-7.
30. Shea, S.D., Koch, H., Baleckaitis, D., Ramirez, J.M., and Margoliash, D. (2010). Neuron-specific cholinergic modulation of a forebrain song control nucleus. J. Neurophysiol. *103*, 733–745. https://doi.org/10.1152/jn.00803.2009.
31. Long, M.A., and Fee, M.S. (2008). Using temperature to analyse temporal dynamics in the songbird motor pathway. Nature *456*, 189–194. https://doi.org/10.1038/nature07448.
32. Long, M.A., Jin, D.Z., and Fee, M.S. (2010). Support for a synaptic chain model of neuronal sequence generation. Nature *468*, 394–399. https://doi.org/10.1038/nature09514.
33. Scotto-Lomassese, S., Rochefort, C., Nshdejan, A., and Scharff, C. (2007). HVC interneurons are not renewed in adult male zebra finches. Eur. J. Neurosci. *25*, 1663–1668. https://doi.org/10.1111/j.1460-9568.2007.05418.x.
34. Colquitt, B.M., Merullo, D.P., Konopka, G., Roberts, T.F., and Brainard, M.S. (2021). Cellular transcriptomics reveals evolutionary identities of songbird vocal circuits. Science *371*, eabd9704. https://doi.org/10.1126/science.abd9704.
35. Kornfeld, J., Benezra, S.E., Narayanan, R.T., Svara, F., Egger, R., Oberlaender, M., Denk, W., and Long, M.A. (2017). EM connectomics reveals axonal target variation in a sequence-generating network. eLife *6*, e24364. https://doi.org/10.7554/eLife.24364.
36. Kosche, G., Vallentin, D., and Long, M.A. (2015). Interplay of inhibition and excitation shapes a premotor neural sequence. J. Neurosci. *35*, 1217–1227. https://doi.org/10.1523/JNEUROSCI.4346-14.2015.
37. Mooney, R., and Prather, J.F. (2005). The HVC microcircuit: the synaptic basis for interactions between song motor and vocal plasticity pathways. J. Neurosci. *25*, 1952–1964. https://doi.org/10.1523/JNEUROSCI.3726-04.2005.
38. Fee, M.S., Kozhevnikov, A.A., and Hahnloser, R.H.R. (2004). Neural mechanisms of vocal sequence generation in the songbird. Ann. N. Y. Acad. Sci. *1016*, 153–170. https://doi.org/10.1196/annals.1298.022.
39. Egger, R., Tupikov, Y., Elmaleh, M., Katlowitz, K.A., Benezra, S.E., Picardo, M.A., Moll, F., Kornfeld, J., Jin, D.Z., and Long, M.A. (2020). Local Axonal Conduction Shapes the Spatiotemporal Properties of Neural Sequences. Cell *183*, 537–548.e12. https://doi.org/10.1016/j.cell.2020.09.019.
40. Cannon, J., Kopell, N., Gardner, T., and Markowitz, J. (2015). Neural Sequence Generation Using Spatiotemporal Patterns of Inhibition. PLoS Comput. Biol. *11*, e1004581. https://doi.org/10.1371/journal.pcbi.1004581.
41. Daou, A., Ross, M.T., Johnson, F., Hyson, R.L., and Bertram, R. (2013). Electrophysiological characterization and computational models of HVC neurons in the zebra finch. J. Neurophysiol. *110*, 1227–1245. https://doi.org/10.1152/jn.00162.2013.
42. Mooney, R. (2000). Different subthreshold mechanisms underlie song selectivity in identified HVc neurons of the zebra finch. J. Neurosci. *20*, 5420–5436. https://doi.org/10.1523/JNEUROSCI.20-14-05420.2000.
43. Wild, J.M., Williams, M.N., Howie, G.J., and Mooney, R. (2005). Calcium-binding proteins define interneurons in HVC of the zebra finch (Taeniopygia guttata). J. Comp. Neurol. *483*, 76–90. https://doi.org/10.1002/cne.20403.
44. Raksin, J.N., Glaze, C.M., Smith, S., and Schmidt, M.F. (2012). Linear and nonlinear auditory response properties of interneurons in a high-order avian vocal motor nucleus during wakefulness. J. Neurophysiol. *107*, 2185–2201. https://doi.org/10.1152/jn.01003.2009.
45. Rauske, P.L., Shea, S.D., and Margoliash, D. (2003). State and neuronal class-dependent reconfiguration in the avian song system. J. Neurophysiol. *89*, 1688–1701. https://doi.org/10.1152/jn.00655.2002.
46. Yildiz, I.B., and Kiebel, S.J. (2011). A hierarchical neuronal model for generation and online recognition of birdsongs. PLoS Comput. Biol. *7*, e1002303. https://doi.org/10.1371/journal.pcbi.1002303.
47. Norton, P., Benichov, J.I., Pexirra, M., Schreiber, S., and Vallentin, D. (2022). A feedforward inhibitory premotor circuit for auditory-vocal interactions in zebra finches. Proc. Natl. Acad. Sci. USA *119*, e2118448119. https://doi.org/10.1073/pnas.2118448119.
48. Vallentin, D., Kosche, G., Lipkind, D., and Long, M.A. (2016). Neural circuits. Inhibition protects acquired song segments during vocal learning in zebra finches. Science *351*, 267–271. https://doi.org/10.1126/science.aad3023.
49. Brainard, M.S., and Doupe, A.J. (2002). What songbirds teach us about learning. Nature *417*, 351–358. https://doi.org/10.1038/417351a.
50. Dave, A.S., and Margoliash, D. (2000). Song replay during sleep and computational rules for sensorimotor vocal learning. Science *290*, 812–816. https://doi.org/10.1126/science.290.5492.812.
51. Elmaleh, M., Yang, Z., Ackert-Smith, L.A., and Long, M.A. (2023). Uncoordinated sleep replay across hemispheres in the zebra finch. Curr. Biol. *33*, 4704–4712.e3. https://doi.org/10.1016/j.cub.2023.09.005.
52. Hahnloser, R.H.R., Kozhevnikov, A.A., and Fee, M.S. (2006). Sleep-related neural activity in a premotor and a basal-ganglia pathway of the songbird. J. Neurophysiol. *96*, 794–812. https://doi.org/10.1152/jn.01064.2005.
53. Elmaleh, M., Kranz, D., Asensio, A.C., Moll, F.W., and Long, M.A. (2021). Sleep replay reveals premotor circuit structure for a skilled behavior. Neuron *109*, 3851–3861.e4. https://doi.org/10.1016/j.neuron.2021.09.021.
54. Kozhevnikov, A.A., and Fee, M.S. (2007). Singing-related activity of identified HVC neurons in the zebra finch. J. Neurophysiol. *97*, 4271–4283. https://doi.org/10.1152/jn.00952.2006.
55. Klausberger, T., Magill, P.J., Márton, L.F., Roberts, J.D.B., Cobden, P.M., Buzsáki, G., and Somogyi, P. (2003). Brain-state- and cell-type-specific firing of hippocampal interneurons in vivo. Nature *421*, 844–848. https://doi.org/10.1038/nature01374.

56. Dimidschstein, J., Chen, Q., Tremblay, R., Rogers, S.L., Saldi, G.A., Guo, L., Xu, Q., Liu, R., Lu, C., Chu, J., et al. (2016). A viral strategy for targeting and manipulating interneurons across vertebrate species. Nat. Neurosci. *19*, 1743–1749. https://doi.org/10.1038/nn.4430.

57. Hofer, S.B., Ko, H., Pichler, B., Vogelstein, J., Ros, H., Zeng, H., Lein, E., Lesica, N.A., and Mrsic-Flogel, T.D. (2011). Differential connectivity and response dynamics of excitatory and inhibitory neurons in visual cortex. Nat. Neurosci. *14*, 1045–1052. https://doi.org/10.1038/nn.2876.

58. Khan, A.G., Poort, J., Chadwick, A., Blot, A., Sahani, M., Mrsic-Flogel, T.D., and Hofer, S.B. (2018). Distinct learning-induced changes in stimulus selectivity and interactions of GABAergic interneuron classes in visual cortex. Nat. Neurosci. *21*, 851–859. https://doi.org/10.1038/s41593-018-0143-z.

59. Ko, H., Hofer, S.B., Pichler, B., Buchanan, K.A., Sjöström, P.J., and Mrsic-Flogel, T.D. (2011). Functional specificity of local synaptic connections in neocortical networks. Nature *473*, 87–91. https://doi.org/10.1038/nature09880.

60. Kerlin, A.M., Andermann, M.L., Berezovskii, V.K., and Reid, R.C. (2010). Broadly tuned response properties of diverse inhibitory neuron subtypes in mouse visual cortex. Neuron *67*, 858–871. https://doi.org/10.1016/j.neuron.2010.08.002.

61. Knott, G.W., Holtmaat, A., Trachtenberg, J.T., Svoboda, K., and Welker, E. (2009). A protocol for preparing GFP-labeled neurons previously imaged in vivo and in slice preparations for light and electron microscopic analysis. Nat. Protoc. *4*, 1145–1156. https://doi.org/10.1038/nprot.2009.114.

62. Baden, T., Berens, P., Franke, K., Román Rosón, M., Bethge, M., and Euler, T. (2016). The functional diversity of retinal ganglion cells in the mouse. Nature *529*, 345–350. https://doi.org/10.1038/nature16468.

63. Geiller, T., Vancura, B., Terada, S., Troullinou, E., Chavlis, S., Tsagkatakis, G., Tsakalides, P., Ócsai, K., Poirazi, P., Rózsa, B.J., and Losonczy, A. (2020). Large-Scale 3D Two-Photon Imaging of Molecularly Identified CA1 Interneuron Dynamics in Behaving Mice. Neuron *108*, 968–983.e9. https://doi.org/10.1016/j.neuron.2020.09.013.

64. Bugeon, S., Duffield, J., Dipoppa, M., Ritoux, A., Prankerd, I., Nicoloutsopoulos, D., Orme, D., Shinn, M., Peng, H., Forrest, H., et al. (2022). A transcriptomic axis predicts state modulation of cortical interneurons. Nature *607*, 330–338. https://doi.org/10.1038/s41586-022-04915-7.

65. Condylis, C., Ghanbari, A., Manjrekar, N., Bistrong, K., Yao, S., Yao, Z., Nguyen, T.N., Zeng, H., Tasic, B., and Chen, J.L. (2022). Dense functional and molecular readout of a circuit hub in sensory cortex. Science *375*, eabl5981. https://doi.org/10.1126/science.abl5981.

66. Cruikshank, S.J., Lewis, T.J., and Connors, B.W. (2007). Synaptic basis for intense thalamocortical activation of feedforward inhibitory cells in neocortex. Nat. Neurosci. *10*, 462–468. https://doi.org/10.1038/nn1861.

67. Markram, H., Toledo-Rodriguez, M., Wang, Y., Gupta, A., Silberberg, G., and Wu, C. (2004). Interneurons of the neocortical inhibitory system. Nat. Rev. Neurosci. *5*, 793–807. https://doi.org/10.1038/nrn1519.

68. Wu, S.J., Sevier, E., Dwivedi, D., Saldi, G.A., Hairston, A., Yu, S., Abbott, L., Choi, D.H., Sherer, M., Qiu, Y., et al. (2023). Cortical somatostatin interneuron subtypes form cell-type-specific circuits. Neuron *111*, 2675–2692.e9. https://doi.org/10.1016/j.neuron.2023.05.032.

69. Chamberland, S., Grant, G., Machold, R., Nebet, E.R., Tian, G., Hanani, M., Kullander, K., and Tsien, R.W. (2024). Functional specialization of hippocampal somatostatin-expressing interneurons. Proc. Natl. Acad. Sci. USA *121*, e2306382121. https://doi.org/10.1073/pnas.2306382121.

70. Green, J., Bruno, C.A., Traunmüller, L., Ding, J., Hrvatin, S., Wilson, D.E., Khodadad, T., Samuels, J., Greenberg, M.E., and Harvey, C.D. (2023). A cell-type-specific error-correction signal in the posterior parietal cortex. Nature *620*, 366–373. https://doi.org/10.1038/s41586-023-06357-1.

71. Muñoz, W., Tremblay, R., Levenstein, D., and Rudy, B. (2017). Layer-specific modulation of neocortical dendritic inhibition during active wakefulness. Science *355*, 954–959. https://doi.org/10.1126/science.aag2599.

72. Muñoz, W., and Rudy, B. (2014). Spatiotemporal specificity in cholinergic control of neocortical function. Curr. Opin. Neurobiol. *26*, 149–160. https://doi.org/10.1016/j.conb.2014.02.015.

73. Sugihara, H., Chen, N., and Sur, M. (2016). Cell-specific modulation of plasticity and cortical state by cholinergic inputs to the visual cortex. J. Physiol. Paris *110*, 37–43. https://doi.org/10.1016/j.jphysparis.2016.11.004.

74. Huang, Z.J., and Paul, A. (2019). The diversity of GABAergic neurons and neural communication elements. Nat. Rev. Neurosci. *20*, 563–572. https://doi.org/10.1038/s41583-019-0195-4.

75. Gouwens, N.W., Sorensen, S.A., Baftizadeh, F., Budzillo, A., Lee, B.R., Jarsky, T., Alfiler, L., Baker, K., Barkan, E., Berry, K., et al. (2020). Integrated Morphoelectric and Transcriptomic Classification of Cortical GABAergic Cells. Cell *183*, 935–953.e19. https://doi.org/10.1016/j.cell.2020.09.057.

76. Vormstein-Schneider, D., Lin, J.D., Pelkey, K.A., Chittajallu, R., Guo, B., Arias-Garcia, M.A., Allaway, K., Sakopoulos, S., Schneider, G., Stevenson, O., et al. (2020). Viral manipulation of functionally distinct interneurons in mice, non-human primates and humans. Nat. Neurosci. *23*, 1629–1636. https://doi.org/10.1038/s41593-020-0692-9.

77. Vandereyken, K., Sifrim, A., Thienpont, B., and Voet, T. (2023). Methods and applications for single-cell and spatial multi-omics. Nat. Rev. Genet. *24*, 494–515. https://doi.org/10.1038/s41576-023-00580-2.

78. Kvitsiani, D., Ranade, S., Hangya, B., Taniguchi, H., Huang, J.Z., and Kepecs, A. (2013). Distinct behavioural and network correlates of two interneuron types in prefrontal cortex. Nature *498*, 363–366. https://doi.org/10.1038/nature12176.

79. Pachitariu, M., Steinmetz, N., Kadir, S., Carandini, M., and Harris, K.D. (2016). Kilosort: realtime spike-sorting for extracellular electrophysiology with hundreds of channels. Preprint at bioRxiv. https://doi.org/10.1101/061481.

80. Rossant, C., Kadir, S.N., Goodman, D.F.M., Schulman, J., Hunter, M.L.D., Saleem, A.B., Grosmark, A., Belluscio, M., Denfield, G.H., Ecker, A.S., et al. (2016). Spike sorting for large, dense electrode arrays. Nat. Neurosci. *19*, 634–641. https://doi.org/10.1038/nn.4268.

81. Stuart, T., Butler, A., Hoffman, P., Hafemeister, C., Papalexi, E., Mauck, W.M., 3rd, Hao, Y., Stoeckius, M., Smibert, P., and Satija, R. (2019). Comprehensive Integration of Single-Cell Data. Cell *177*, 1888–1902.e21. https://doi.org/10.1016/j.cell.2019.05.031.

82. Chaure, F.J., Rey, H.G., and Quian Quiroga, R. (2018). A novel and fully automatic spike-sorting implementation with variable number of features. J. Neurophysiol. *120*, 1859–1871. https://doi.org/10.1152/jn.00339.2018.

83. Benezra, S.E., Narayanan, R.T., Egger, R., Oberlaender, M., and Long, M.A. (2018). Morphological characterization of HVC projection neurons in the zebra finch (Taeniopygia guttata). J. Comp. Neurol. *526*, 1673–1689. https://doi.org/10.1002/cne.24437.

84. Picardo, M.A., Merel, J., Katlowitz, K.A., Vallentin, D., Okobi, D.E., Benezra, S.E., Clary, R.C., Pnevmatikakis, E.A., Paninski, L., and Long, M.A. (2016). Population-Level Representation of a Temporal Sequence Underlying Song Production in the Zebra Finch. Neuron *90*, 866–876. https://doi.org/10.1016/j.neuron.2016.02.016.

85. English, D.F., McKenzie, S., Evans, T., Kim, K., Yoon, E., and Buzsáki, G. (2017). Pyramidal Cell-Interneuron Circuit Architecture and Dynamics in Hippocampal Networks. Neuron *96*, 505–520.e7. https://doi.org/10.1016/j.neuron.2017.09.033.

86. Stark, E., and Abeles, M. (2009). Unbiased estimation of precise temporal correlations between spike trains. J. Neurosci. Methods *179*, 90–100. https://doi.org/10.1016/j.jneumeth.2008.12.029.

STAR★METHODS

KEY RESOURCES TABLE

REAGENT or RESOURCE	SOURCE	IDENTIFIER
Antibodies		
mouse anti-PV	Sigma Aldrich	Cat# P3088; RRID:AB_477329
rabbit anti-SST	Peninsula Laboratories	Cat# T-4103; RRID:AB_518614
donkey anti-rabbit Alexa 594	Thermo Fisher Scientific	Cat# A32754; RRID:AB_2762827
donkey anti-mouse Alexa 405	Thermo Fisher Scientific	Cat# A48257; RRID:AB_2884884
Bacterial and virus strains		
pAAV-mDlx-GFP-Fishell-1	Addgene; Dimidschstein et al.[56]	RRID:Addgene_83900
Chemicals, peptides, and recombinant proteins		
Red Retrobeads	Lumafluor, Inc.	N/A
Dextran, Tetramethylrhodamine, 70,000 MW, Lysine Fixable	Thermo Fisher Scientific	D1818
Alexa Fluor 594 Hydrazide	Thermo Fisher Scientific	A10438
Critical commercial assays		
Chromium Single Cell 3′ v3 Reagent Kit	10x Genomics	PN 1000075
High Sensitivity DNA Kit	Agilent	5067-4626
DAPI staining solution	abcam	ab228549
Bovine Serum Albumin	Sigma-Aldrich	A4161
Experimental models: Organisms/strains		
Zebra finch (Taeniopygia guttata)	Magnolia Bird Farm, Anaheim, CA	N/A
Software and algorithms		
MATLAB 2022a	Mathworks	https://www.mathworks.com/products/matlab.html
KiloSort	Pachitariu et al.[79]	https://github.com/cortex-lab/KiloSort
Phy2	Rossant et al.[80]	https://github.com/cortex-lab/phy
R 3.6.3	Comprehensive R Archive Network	https://cran.r-project.org/
RStudio Builds 353	Posit	https://posit.co/download/rstudio-desktop/
Seurat package	Stuart et al.[81]	https://satijalab.org/seurat/
ScanImage 4.2 (2015)	Vidrio Technologies	https://www.mathworks.com/products/connections/product_detail/scanimage.html
Axon pCLAMP electrophysiology software	Molecular Devices	pCLAMP 10.7.0
Wave_clus 3	Chaure et al.[82]	https://github.com/csn-le/wave_clus
FIJI	ImageJ Wiki	https://imagej.net/software/fiji/downloads
Other		
High-density silicon probe (with integrated headstage)	Diagnostic Biochips	128-5 integrated
Audio amplifier	Presonus	Studio Channel
Acquisition board	Intan Technologies	RHD Recording Controller (512 channels)
Omnidirectional microphone	Audio-Technica	AT803
Nanoject III	Drummond Scientific	https://shop.drummondsci.com/products/nanoject-iii
Ti:sapphire laser	Chameleon, Coherent	https://www.coherent.com/lasers/oscillators/chameleon-ultra
Intracellular recording amplifier	Molecular Devices	Multiclamp 700B
Digital acquisition board	Molecular Devices	Axon Digidata 1550
Isolated Pulse Stimulator	A-M Systems	Model 2100
Digital signal processor	Tucker-Davis Technologies	RX8

(*Continued on next page*)

Continued

REAGENT or RESOURCE	SOURCE	IDENTIFIER
Master-9 Stimulator	A.M.P.I.	9-channel stimulator
Resonant scanner	Thorlabs	N/A
Movable Objective Microscope	Sutter Instrument Company	N/A
20X Olympus Water Immersion Objective	Olympus	N20X-PFH
Pockels Cell	ConOptics	302RM
GaAsP photomultiplier tubes	Hamamatsu	H10770PA-40 PMT
Horizontal micropipette puller	Sutter Instruments	P-97
Borosilicate Glass (with filament)	Sutter Instruments	BF150-86-10
D263 Coverslip Glass, 3 mm diameter, #0 thickness	Warner Instruments	64-0726; CS-3R-0
Glass window customization for juxtacellular recordings	Potomac Photonics	N/A
CMOS Camera	Point Grey	Grasshopper3
MoFlo XDP Cell Sorter	Beckman Coulter	N/A
Bioanalyzer Instrument	Agilent	N/A
Chromium Controller	10X Genomics	Chromium X

EXPERIMENTAL MODEL AND STUDY PARTICIPANT DETAILS

For all experiments, we used adult (>90 days posthatch) male zebra finches (*Taeniopygia guttata*) obtained from an outside breeder and maintained in a temperature- and humidity-controlled environment with a 12/12 h light/dark schedule. A subset of finches used in these experiments were acclimated to a shifted light schedule for a minimum of 7 days to alter the natural onset time of sleep for chronic recordings. Undirected singing behavior for each finch was recorded in a custom sound isolation chamber using an omni-directional microphone (Audio-Technica) connected to an analog preamplifier (Presonus). All animal maintenance and experimental procedures were performed according to the guidelines established by the Institutional Animal Care and Use Committee at the New York University Langone Medical Center, and facilities were inspected by the veterinary staff twice weekly.

METHOD DETAILS

Surgical approaches

Surgical setup

Finches were anesthetized under isoflurane (1.5%-3% in oxygen) and placed in a stereotactic device with a temperature-controlled heat pad to maintain body temperature throughout the surgery. Following all procedures, analgesia was introduced both systemically and locally at incision sites to mitigate pain, and animals were checked every 12 h for 3 days following surgery.

Stereotactic microinjections

During surgery, injections of viruses or fluorescent tracers were performed in the right hemisphere using a microinjector (Nanoject 3, Drummond Scientific) via a sharp glass pipette at a rate of 20 nL/min which was left in place for 2-3 min post-injection to minimize backflow of virus during pipette removal. rAAV-mDlx-GFP[56] (Addgene: pAAV-mDlx-GFP-Fishell-1, Plasmid # 83900) was injected through a small craniotomy and durotomy (∼0.1 mm A-P, ∼0.4 mm M-L) centered on HVC (0.25 mm anterior and 2.3 mm lateral to the bifurcation of the sagittal sinus). Three injections total were performed at 2.1/2.3/2.5 mm (150 nL in each location), each at a depth of 400-450 μm. A fluorescent retrograde tracer (Red Retrobeads, Lumafluor, Inc.) was injected into Area X (5.8 mm anterior and 1.5 mm lateral to the bifurcation of the sagittal sinus). Injections were made at a depth of 2.8 mm at three angles (-5°, 0°, +5°). In some cases, the Red Retrobeads were diluted 3:5 (beads:saline) to avoid blockage of the injection pipette. After injections were performed, the craniotomy was covered with silicon elastomer (Kwik-Cast, WPI).

Implantations

During surgery, various items were affixed to the skull as dictated by experimental need. Silicon probes (Diagnostic Biochips, 128-5) were implanted into HVC on the right hemisphere as described previously.[39,53] To enable head-fixed imaging *in vivo*, a metal headplate was secured to the anterior portion of the skull using dental acrylic (A-M Systems) either 3 weeks post-injection (i.e., at peak expression of the virus) for juxtacellular experiments or immediately following dextran injection for whole-cell experiments. One day prior to imaging, a borosilicate cranial window was implanted to facilitate two-photon guided recordings of labeled neurons. Cranial windows consisted of a circular disc (#0 thickness, 3 mm diameter, Warner Instruments) or a custom coverslip with a rectangular open slit (0.3 mm X 1.5 mm, 30-degree incline on the long edge, Potomac Photonics). Immediately before implantation, the craniotomy was enlarged (edge length: ∼0.5-1.0 mm), and in some cases the dura and hippocampal tissue overlying HVC were removed.

Cranial windows were affixed to the inner skull with cyanoacrylate around the edges and further secured with dental acrylic (A-M Systems) on the perimeter.

Tissue harvesting for sequencing

During surgery, HVC tissue was harvested for transcriptomic analysis. Two large (1 mm X 1 mm) craniotomies were formed above HVC, and the dura and hippocampus directly above HVC were removed. Using a small scoopula under stereotaxic control the bulbous HVC nuclei were bilaterally scooped out of the brain and immediately placed into liquid nitrogen for flash freezing. Following HVC removal, the finch was humanely euthanized per standard procedures.

Experimental approaches

Two-photon imaging

Two-photon imaging was used to target fluorescently labeled HVC neurons with a glass pipette for either whole-cell or juxtacellular recordings. As described elsewhere,[35,83,84] the microscope (MOM, Sutter Instruments) was controlled using ScanImage 2015a with a moveable 20X/1 NA water immersion objective (Olympus). The excitation source was a Ti:sapphire laser (Chameleon, Coherent), controlled by a Pockels cell (Conoptics 302RM) and tuned to either 870 nm to optimize simultaneous visualization of GFP, Retrobeads, and Alexa 594 or 800 nm to simultaneous visualize Dextran Alexa 488 and Alexa 594. GaAsP photomultiplier tubes (H10770PA-40 PMT module) were used to detect fluorescent light.

Whole-cell recordings

Targeted whole-cell recordings were performed on HVC excitatory projection neurons to visualize synaptic currents in unanesthetized birds. First, birds were head-fixed and placed in a foam restraint so that retrogradely labeled neurons projecting to Area X could be localized using two-photon microscopy. Then, under isoflurane anesthesia, a rectangular hole (~0.25 mm x 0.25 mm) was carefully drilled in the cranial window lateral to the target cells using a carbide needle bur (HM246-008, Meisinger). Patch pipettes were pulled from filamented borosilicate glass (ID: 0.86 mm, OD: 1.5 mm, Sutter Instrument) and filled with an internal solution containing (in mM): 130 Cs-Gluconate, 4 CsCl, 2 NaCl, 10 HEPES, 0.2 EGTA, 14 phosphocreatine-Tris, 4 MgATP, 0.3 GTP-Tris (pH balanced to 7.25 ± 0.05 with CsOH; final osmolality 300 ± 5 mOsm) with 7.5 μM Alexa 594 added on day of experiment for visualization. Final tip resistance was 3.5-5.5 MΩ, and a -14 mV junction potential was corrected in all experiments.

Recording sessions were initiated at least 30 min following recovery from anesthesia. Birds were returned to the two-photon microscope, and a dental acrylic well surrounding the entry point in the optical window was filled with sterile saline. Patch pipettes were guided into the hole in the cranial window using a motorized micromanipulator (Luigs & Neumann) under ~200 mbar of positive pressure. Positive pressure was reduced to 70-90 mbar upon penetration into HVC, and further reduced to 15-30 mbar when the pipette tip was within 100-150 μm of the target cell. Contact with the membrane of the target neuron was determined visually and associated with a 0.3-1 MΩ increase in tip resistance. Positive pressure was quickly released upon contact with the membrane to form a GΩ seal. Whole-cell access was achieved using brief pulses of negative pressure, after which compensation for whole-cell capacitance and series resistance was performed. Series resistance was compensated 30%-85% in all experiments and uncompensated series resistances ranged from 10-40 MΩ across cells. Neurons were clamped at the excitatory reversal potential (1.4 ± 3.5 mV) to isolate inhibitory postsynaptic currents. Whole-cell currents were amplified (Multiclamp 700B), digitized (Digidata 1550B), low-pass filtered at 10 kHz, and sampled at 50 kHz (pClamp 10.7; Molecular Devices). Recordings were held for several minutes under both lights ON and lights OFF conditions to assay for arousal-based changes in spontaneous inhibitory synaptic activity and to measure inhibitory responses evoked by song playback in the lights ON condition.

Silicon probe recordings

Silicon probe recordings were carried out in a manner consistent with our group's previous publications.[39,53] Briefly, zebra finches were connected to an electrically assisted commutator (Doric Lenses) to enable free movement. Custom sound attenuating recording boxes were equipped with cameras to visually monitor behavior, a speaker for song playback, and an omnidirectional microphone (Audio-Technica) connected to an analog preamplifier (Presonus) for recording song production. Electrophysiological recordings lasted between 3 and 14 h and included periods of exposure to a female zebra finch in an adjacent cage to elicit directed song as well as periods in which lights were turned off. Additionally, 25 to 100 trials of song playback were introduced during the lights ON period. Audio, light luminance, and neural data were all acquired using the RHD Intan Recording Controller.

Tissue dissociation

Tissue was transferred into Extraction Buffer, consisting of Dissociation Media + 1% Kollidon VA64 + 1% Triton X-100 + 1:100 RNase-inhibitor + FITC-conjugated NeuN for future sorting, and triturated 20 times every 2.5 min for 10 min. Suspension was aspirated with a pre-chilled 27G needle and released across a 6-well plate to further dissociate larger chunks of tissue. This product was further strained through a 100 μM filter into four 50 mL tubes with Dissociation Media and centrifuged at 550 rcf for 10 min at 4°C. Supernatant was removed and pellets were combined and strained through a final 75 μM filter. For cell sorting, 1 μL/1 mL DAPI and 0.1-1% nuclease-free Bovine Serum Albumin was added to the volume.

Nuclei sorting and sequencing

Samples were run on a MoFlo XDP for FAC Sorting, enriching for DAPI+ and FITC+ nuclei. Post FACS, nuclei were sent to NYU Langone Genome Technology Center for 10X single-nuclei sequencing. Single nuclei were encapsulated into emulsion droplets using Chromium Controller (10x Genomics). scRNA-seq libraries were constructed using Chromium Single Cell 3′ v3 Reagent Kit (PN 1000075) according to the manufacturer's protocol. Amplified cDNA was evaluated on an Agilent BioAnalyzer 2100 using a

High Sensitivity DNA Kit and final libraries were assembled on an Agilent TapeStation 4200 using High Sensitivity D1000 ScreenTape (Agilent Technologies). Individual libraries were diluted to 2 nM and pooled for sequencing; pools were sequenced according to manufacturer recommendations.

Juxtacellular recordings

Following window implantation, birds were left to recover with food and water for at least 2 h, but usually overnight, before recordings took place. In a few initial experiments, Dextran Tetramethylrhodamine (70,000 MW; diluted 40 μL into 160 μL sterile saline) was injected intraperitoneally into the chest cavity (left of midline, between lower ribs) to label blood vessels and aid with relocating cells in histology. Pipettes were fabricated from borosilicate glass with filament (O.D. 1.5 mm; I.D. 0.86 mm) using a horizontal puller (P97, Sutter Instruments) and loaded with internal solution consisting of sterile saline and Alexa 594 dye (40 μM) to visualize the pipette, yielding a final resistance of 3-6 MΩ. Birds were placed in a foam restraint and head-fixed under the two-photon microscope. The recording pipette was guided to GFP-positive cells under two-photon visualization and spikes were recorded in a juxtacellular configuration. Juxtacellular signals were amplified (Multiclamp 700B), digitized (Digidata 1550B), low-pass filtered at 10 kHz, and sampled at 50 kHz (pClamp 10.7; Molecular Devices).

GFP-positive cells that had any bead labeling were not approached, as these cells were rare and likely due to leakage of the virus into excitatory populations. Each cell was recorded for several minutes under lights ON and lights OFF periods to best emulate conditions of the silicon probe recordings in this head-fixed imaging setup. Each recording included trials of song motif playback in both light conditions coming from a speaker, with a microphone (Audio-Technica) placed equidistant from the speaker and the bird, which was amplified (Presonus). To monitor the vigilance state of the birds during each recording session, we used a CMOS camera (Point Grey Grasshopper3) to film the bird's contralateral (left) eye at a rate of 4 Hz, which was synced to the physiology with a trigger pulse (Master-9). Camera trigger signal and amplified audio signal were digitized and acquired with the same system as the neural data (Axon Instruments Digidata 1550B). For each bird, a two-photon image stack of the field of view was taken at the beginning of the session to help localize cell populations visualized *in vivo* again in histology (more details on histological processing below). For every cell recorded, an image of the pipette approaching the recorded neuron was recorded with the ScanImage software, along with two image stacks after the recording was complete: one zoomed in (usually 5X) to focus on cell's morphology and one zoomed out (usually 2X) to facilitate post hoc image registration and localization of the recorded cell in histology.

Tangential slicing

After recordings were completed, finches were euthanized with Euthasol (Virbac) and transcardially perfused with 4% paraformaldehyde (PFA). Brains were extracted from the skull and submerged in 4% PFA overnight before being rinsed with 1X PBS for slicing. To optimize chances of localizing the recorded cells in post-hoc histology, brains were mounted on a vibratome (VT1200S; Leica) and covered with 3% agarose for slicing, parallel to the two-photon imaging plane. More specifically, the right hemisphere was placed at an angle that most closely matched the angle of the imaging plane *in vivo* with respect to the blade used for sectioning. We further took advantage of the flattened surface of HVC due to the glass window implant to position the hemisphere properly. Tangential slices were sectioned at 50 μm and submerged in 1X PBS in a 24-well plate for subsequent immunohistochemistry.

Immunohistochemistry

Floating sections were incubated in blocking buffer (10% normal donkey serum in PBS, 0.3% Triton-X, plus 3% bovine serum albumin in some cases) on a rocker for 1 h at room temperature. Slices were then incubated in primary solution (1:1000 mouse anti-PV, Sigma Aldrich P3088) and 1:1000 rabbit anti-SST (BMA Biomedicals T-4103) in blocking buffer) in 4°C on a rocker, covered, for 3 nights. On day 4, slices were washed at least 3 times in 1X PBS every 15 min and subsequently submerged in secondary solution: 1:1000 donkey anti-mouse Alexa 405 and 1:1000 donkey anti-rabbit Alexa 594 (Thermo Fisher Scientific) in blocking buffer and covered to incubate on a rocker either at room temperature for 2 h or in 4°C overnight. Slices were again rinsed at least 3 times in 1X PBS before being mounted on glass microscope slides with MOWIOL mounting medium. Confocal image stacks were acquired using a Zeiss LSM800 microscope with 20X and 40X oil-immersion objectives.

Image registration

To identify the molecular profile of cells recorded *in vivo* in processed slices, confocal (histology) and two-photon (*in vivo*) image stacks were registered. This process of manually registering the stacks took a few minutes to several days per bird, depending on how well-aligned the tangential slicing plane was to the *in vivo* imaging plane. Large blood vessels, injection sites, and any other landmark features of the neuropil, such as areas with more red background from the pipette's Alexa dye, were initially used to find the general vicinity of the recorded area. Once a candidate cell was found within this region that matched the morphology and spatial location with respect to these landmarks, the constellation of GFP+ and/or beaded cells surrounding the candidate also had to match in both imaging stacks for the cell to be counted as 'recovered'.

Whole-cell analysis

Preprocessing of current traces

Visualization and initial analysis of voltage clamp data were performed using Clampfit (pClamp 10.7, Molecular Devices). Periods where series resistance was > 40 MΩ or when the quality of the seal was actively being tested were eliminated from further analysis. Holding current was subtracted by computing a set of baseline anchor points in each 2-s window (1-s steps) by estimating the probability density function of the current values using kernel density estimation (ksdensity). The baseline anchor point for a specific

window is the value of current for which the empirical cumulative density function equals 0.05. A cubic spline was used to connect all anchor points into a continuous, nonlinear baseline.

Calculating playback-evoked mean IPSC

For each cell (n = 10), the mean playback evoked current was computed for every instance of playback. The window for playback evoked current extended 0.5 s after the end of the audio stimulus. The mean baseline current for each cell and playback event was computed via bootstrapping. Random (n = 1000) intervals of current in a 10-s window preceding each playback event, and whose duration matches the respective playback evoked segment were averaged. The mean and standard deviation of baseline currents across all playback events were calculated for each cell.

Compound inhibitory events

A threshold that distinguishes elevated levels of inhibitory current was defined for each cell as the 10th percentile value of current within 10 s intervals. Compound inhibitory events were defined to be intervals exceeding 100 ms, for which the current exceeded the threshold. The standard deviations of the frequency of compound events, during lights ON and OFF, were computed using bootstrapping with parameters: p = 0.35, n = 10000.

Silicon probe analysis

Auditory signal processing

To analyze auditory signals, we used custom MATLAB software to detect both song and playback trials, with sample-matched precision with the neural data. These audio timestamps were used for all song and song playback spike alignment. Playback spiking was calculated with a 30-ms delay after the beginning and end of the motif, to account for auditory processing.[47] Any awake playback trial containing female call contamination from the adjacent cage was discarded. All periods outside of singing and playback trials (with a 500-ms buffer) were considered spontaneous activity.

Spike detection and single-unit clustering

As described previously,[39,53] we used Kilosort 1[79] software for automated spike sorting and clustering of units collected through silicon probe recordings. We performed manual post-processing with Phy[80] to ensure units were stable across time and had self-similar waveforms occupying a consistent spatial distribution across channels.

Classifying putative cell types

To systematically differentiate excitatory projection cells from interneurons, we calculated the trough-to-peak rise time of the mean waveform of 2000 randomly chosen spikes and the song sparsity index (i.e., the proportion of 5-ms bins of song PSTHs that had zero spiking activity across trials) for each unit. We used k-means clustering to distinguish the two populations (Figure 1F) and then applied an additional criterion (i.e., cross-correlation analysis) to confirm these designations (sections below).

Cross-correlograms and curve fitting

Cross-correlograms (CCGs) representing putative excitatory or inhibitory connections were computed for each pair of isolated units in each bird regardless of the position of the spike waveform on the recording array. All CCGs analyzed had a bin width of 0.2 ms. To reduce the possibility of spurious correlations resulting from correlated inputs, we excluded spiking activity during song motif production in awake finches as well as song playback during both wakefulness and sleep.

Putative excitatory connections

The lower frequency baseline, λ_{slow}, was calculated by convolving the CCG with a "hollow" Gaussian kernel,[85,86] with a standard deviation of 0.5 ms, hollow fraction of 60%, and a hollow duration of 0.2 ms. Two criteria were required (Figure S1), (1) for some lag m $\in$ [0.5, 2.5] ms, $P_{fast} < 10^{-6}$, (2) for some lag m $\in$ [-0.5, -2.5] ms, $P_{causal} < 10^{-5}$. Due to the noisiness of relatively low-count CCGs, additional criteria were imposed using curve fitting. If a CCG met criteria (1) and (2), its portion in lags [0, 5] ms was curve fit—using MATLAB 2022a, fitnlm—to a double exponential function of the form:

$$f_e(t) = \frac{k}{e^{-a(t-c)}+e^{b(t-c)}} + d$$

CCGs were converted from counts to mean firing rate before curve fitting. Three additional criteria were required, (3) a goodness of fit, $R^2 > 0.5$, (4) narrowness of peak, a > 1.5 and b > 1.5, and (5) height of peak, k > 20. A CCG was classified as a putative excitatory connection if all five criteria were satisfied and was excluded from the following screenings.

Putative inhibitory connections

Since the baseline correction method[85] does not detail the identification of putative inhibitory connections, P_{fast} and P_{causal} were modified to detect CCGs significantly below λ_{slow}. The hollow Gaussian had a standard deviation of 2 ms, hollow fraction of 60%, and a hollow duration of 0.4 ms. Two criteria were required, (1) for some lag m $\in$ [0.5, 2.5] ms, $P_{fast} < 10^{-4}$, (2) for some lag m $\in$ [-0.5, -2.5] ms, $P_{causal} < 10^{-6}$. If both criteria were met, the CCG was fit to $f_i(t)$, given by:

$$f_i(t) = f_e(t) + k_i \cdot e^{a_i t}$$

Three more criteria were, (3) a dipped $f_e(t)$, $k < -0.5$, (4) quickly descending and slowly ascending, $a > 4$ and $b > 1.5$, and (5) short latency trough, defined by the global minima of $f_e(t)$ at t $\in$ [0.5, 2.5] ms. If all five criteria were met, and not already classified as either of the two cases described above, the CCG was deemed as representing a putative inhibitory connection.

Many CCGs exhibited a tall peak surrounding 0 ms lag (Figure S1), representing highly synchronous activity, and likely a result of common excitatory input or electrical coupling. The rapidly descending shape of such CCGs were often wrongly identified as candidates for putative inhibitory connections. Thus, such zero-lag CCGs were algorithmically classified using the baseline correction method and curve fitting to a difference of Gaussians function. The hollow Gaussian kernel had a standard deviation of 1 ms, hollow fraction of 60%, and a hollow duration of 0.4 ms. If (1) for some lag m ∈ [-1, 1] ms, $P_{fast} < 10^{-5}$, the CCG was curve fit to the function:

$$f_s(t) = c_+ \cdot e^{-\left(\frac{t-\mu_+}{\sigma_+}\right)^2} - c_- \cdot e^{-\left(\frac{t-\mu_-}{\sigma_-}\right)^2} + d$$

Two additional criteria were required, (2) a goodness of fit, $R^2 > 0.7$, and (3) global maxima of $f_s(t)$ at t ∈ [-1, 1] ms. If all three criteria were satisfied, the CCG was excluded from the analysis of putative inhibitory connections.

Metrics for putative interneurons

For quantification of spontaneous activity, we used 50 randomized trials of 5-s snippets throughout spontaneous activity periods for lights ON and OFF conditions. Song, playback, and spontaneous firing rates (FR) were calculated as the mean rates across trials of spiking activity. Rate change values for song and playback modulation were calculated as the difference of the firing rate from baseline over the sum with baseline. 'Baseline' for playback activity was defined as the period exactly preceding the playback start time, equal to the length of the song. Given that natural singing often comprises song motifs in rapid succession, we used the mean lights ON spontaneous rate as 'baseline' for singing modulation calculations. ISI correlations (used to measure state-dependent shifts in firing patterns) were calculated as the mean correlation coefficient across histogram bin counts (0.1 ms) for lights ON and lights OFF ISIs. r-to-Z Fisher transformations of correlation-based metrics were made to normalize data for subsequent k-means clustering, using the inverse hyperbolic tangent; correlation values of 1 were set to 0.99 prior to transformation to avoid extreme outliers in distributions.

Transcriptomics analysis

Preprocessing and QC of raw reads

Processing and analysis of our annotated 10X single-cell libraries was conducted using the Seurat[81] package (version 3.1.4) in R (version 3.6.3) and RStudio (Builds 353) software (Seurat toolkit commands referenced below). Cells from each of the data sets were loaded as a Seurat object, with an initial minimum requirement of 200 features (genes) per cell. Datasets were merged (Figure S3E) and subject to quality control measures. Specifically, we required a minimum number of 500 unique genes per cell to prevent analysis of low-quality cells, with an upper limit of 6,000 unique genes to avoid doublet reads. We removed any cells with greater than 1.5% mitochondrial transcripts, filtering for damaged or dying cells. Gene expression measurements were then normalized by the total transcripts detected for each cell and multiplied by a scaling factor of 10,000 before log-transformation.

Dimensionality reduction of transcriptomes

We identified the 2000 most variable features—a subset of genes that have a high degree of variability in expression levels across cells (FindVariableFeatures, selection.method = "vst"). Then we applied a linear transformation to scale the data before dimensionality reduction. We ran principal component analysis (PCA) on the variable features. We determined the dimensionality of the data set using a Jack Straw-based resampling method, scoring the top 60 PCs to find which are significant. We used a graph-based clustering approach on the top 55 PCs that we found to be significant. Using FindNeighbors, we constructed a K-nearest neighbors graph with nodes of highly interconnected communities based on Euclidean distances in PC space. From this graph, we clustered the cells with the Louvain algorithm as the modularity optimization technique and low resolution for broadly grouped clusters (resolution = 0.1, n.start = 10). Next, we ran Uniform Manifold Approximation and Projection (UMAP) as a nonlinear dimensionality reduction technique to be able to visualize our clustered data set in two dimensions (min.dist = 0.75). To find the topmost differentiating markers of each cluster, we used FindAllMarkers to assay the features with the most significantly positive expression in at least 25% of cells of that cluster (logfc.threshold = 0.25).

Clustering analysis of GABAergic cells

We isolated clusters with significant expression levels of GABAergic markers (GAD1, GAD2, and SLC32A1). These clusters were combined into a single data set and re-clustered after dimensionality reduction with the same methodology as before, with slightly tuned parameters for this smaller data set (reduction = 'pca', dims = 1:15, resolution = 0.25, n.start = 10). The resolution was set to obtain the optimal number of clusters (8), as determined by Silhouette analysis.

Juxtacellular analysis

Spike detection

Juxtacellular records were high-pass filtered at 200 Hz to stabilize baselines for spike detection. Spike waveform detection for each interneuron was performed using the Wave_clus 3 Matlab package.[82] Wave_clus parameters were set to analyze negative or positive deflecting spikes depending on the recording's waveform shape (detection = 'neg'/'pos'). A low threshold was set for refractory periods to avoid missed spikes (ref_ms = .5). Spike detection standard deviations ranged from 3 to 5 (stdmin = 3-5), depending on the signal quality of the recording. Waveforms were clustered (features = 'pca'; min_clus = 20; max_clus = 15) using ±40 sample points (w_pre/w_post = 40) around detected spike times (detect_fmin = 200; detect_fmax = 10,000). For each cell, overlayed spike

waveforms, ISI histograms, and cell vs. noise clusters) were visually inspected to remove noisy outliers or occasional spike contaminants from nearby cells.

Parameter calculations for GFP+ interneurons

Metrics characterizing mean waveforms, event-aligned activity, and other aspects of cell profiles were standardized across electrophysiological techniques to the best of our abilities and reported in the 'metrics for putative interneurons' section in the silicon probe analysis methods above, with any differences reported here. Given the shorter recording times, mean waveforms were calculated based on 200 randomly chosen spikes for juxtacellular recordings. Playback responses from the lights OFF condition were used for analysis, plotted as the absolute change in rate (e.g., Figure 4G). The number of random spontaneous activity trials equaled the number of playback trials for each lighting condition (i.e., lights ON and OFF). Spontaneous activity was defined as times outside of playback trials (with a 0.5 s buffer after each motif).

Distance measurements of interneuron subtypes

A distribution of pairwise Euclidean distances in the three-dimensional functional parameter space, between all juxtacellularly recorded interneurons, was computed as a null distribution (Figure 4G). In addition, the same distribution was computed for PV-PV, PV-SST, and SST-SST pairs. To determine the significance of clustering, a Wilcoxon rank sum test was used between pairs of distributions to determine the p value.

QUANTIFICATION AND STATISTICAL ANALYSIS

All statistical details of experiments can be found in figure legends and the results section, including the statistical tests used, exact value of n and what n represents (e.g., number of animals, number of cells, etc.). Values are reported as mean ± SD unless mentioned otherwise, and values are plotted as mean with error bars representing SD unless mentioned otherwise. Significance was defined at a level of 0.05. Normal distribution of data was not assumed. No data were excluded from analysis. Statistical calculations were performed using MATLAB R2022a.